This article has been accepted for publication in IEEE Transactions on Biomedical Circuits and Systems. This is the author's version which has not been fully edited and content may change prior to final publication. Citation information: DOI 10.1109/TBCAS.2024.3372571

A Wireless Multimodal Physiological Monitoring ASIC for Animal Health Monitoring Injectable Devices

Linran Zhao[1*], *Graduate Student Member*, *IEEE*, Raymond G Stephany[1*], Yiming Han[1], *Graduate Student Member*, *IEEE*, Parvez Ahmmed[2], *Member*, *IEEE,* Tzu-Ping Huang[1], *Graduate Student Member*, *IEEE*, Alper Bozkurt[2], *Senior Member*, *IEEE*, Yaoyao Jia[1], *Member*, *IEEE*

[*]Equally Contributed Authors

***Abstract*— Utilizing injectable devices for monitoring animal health offers several advantages over traditional wearable devices, including improved signal-to-noise ratio (SNR) and enhanced immunity to motion artifacts. We present a wireless application-specific integrated circuit (ASIC) for injectable devices. The ASIC has multiple physiological sensing modalities including body temperature monitoring, electrocardiography (ECG), and photoplethysmography (PPG). The ASIC fabricated using the CMOS 180 nm process is sized to fit into an injectable microchip implant. The ASIC features a low-power design, drawing an average DC power of 155.3 µW, enabling the ASIC to be wirelessly powered through an inductive link. To capture the ECG signal, we designed the ECG analog frontend (AFE) with 0.3 Hz low cut-off frequency and 45-79 dB adjustable midband gain. To measure PPG, we employ an energy-efficient and safe switched-capacitor-based (SC) light emitting diode (LED) driver to illuminate an LED with milliampere-level current pulses. A SC integrator-based AFE converts the current of photodiode with a programmable transimpedance gain. A resistor-based Wheatstone Bridge (WhB) temperature sensor followed by an instrumentation amplifier (IA) provides 27–47 ℃ sensing range with 0.02 ℃ inaccuracy. Recorded physiological signals are sequentially sampled and quantized by a 10-bit analog-to-digital converter (ADC) with the successive approximation register (SAR) architecture. The SAR ADC features an energy-efficient switching scheme and achieves a 57.5 dB signal-to-noise-and-distortion ratio (SNDR) within 1 kHz bandwidth. Then, a back data telemetry transmits the baseband data via a backscatter scheme with intermediate-frequency assistance. The ASIC's overall functionality and performance has been evaluated through an *in vivo* experiment.**

Keywords*— *animal health monitoring, injectable device, multimodal sensing, subcutaneous implant, electrocardiography, photoplethysmography, temperature measurement

This work was supported by the United States National Science Foundation (NSF) under Grant ECCS-2151788, Grant ECCS-2239915, Grant IIS-2319060, Grant IIS-2037328, Grant EF-2319389, Grant CCSS-1554367, and Grant ECC-1160483 (NSF Nanosystems Engineering Research Center for Advanced Self-Powered Systems of Integrated Sensors and Technologies (ASSIST)).

L. Zhao, R. G. Stephany, Y. Han, T. Huang, and Y. Jia are with the Chandra Family Department of Electrical and Computer Engineering, The University of Texas at Austin, Austin, TX 78712, USA (e-mail: lrzhao@utexas.edu and yjia@austin.utexas.edu).

P. Ahmmed and A. Bozkurt are with the Department of Electrical and Computer Engineering, North Carolina State University, Raleigh, NC 27695, USA (pahmmed@ncsu.edu and aybozkur@ncsu.edu).

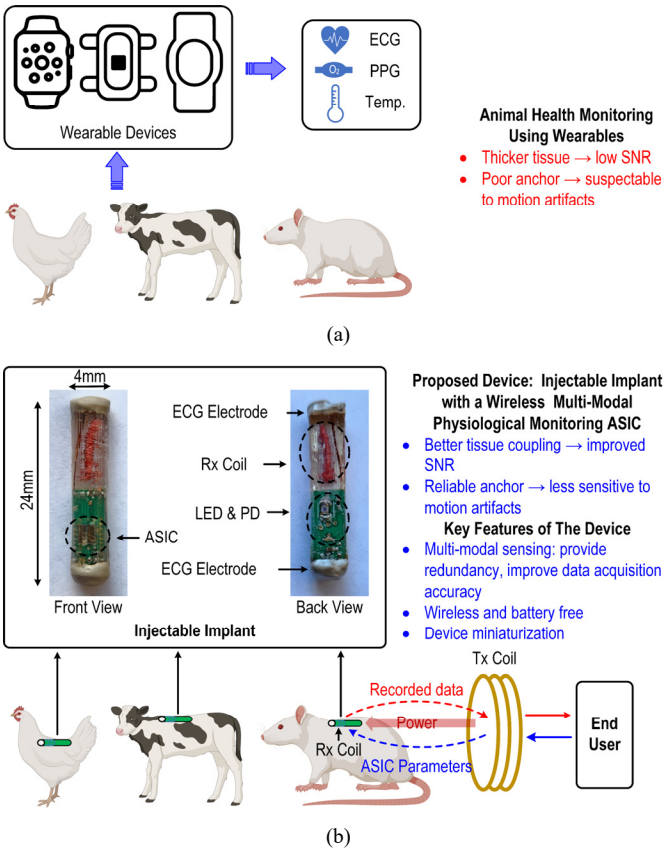

Fig. 1. (a) Challenges of using wearable devices to monitor animal health and (b) the prototype of injectable device enhanced by the wireless multi-modal physiological monitoring ASIC.

I. Introduction

MONITORING animals' health in farms and veterinary clinics requires measuring vital signals such as electrocardiography (ECG), photoplethysmography (PPG), and body temperature [1]-[5]. Wearable devices like smartwatches, chest patches, and wristbands have facilitated personalized health monitoring and health profile creation in humans [6]-[10]. However, when these are used on animals, wearables face several challenges, as shown in Fig. 1a. First, animals typically have thicker skin, which leads to poor coupling between wearable devices and tissue, resulting in weak received signals and compromised signal-to-noise ratio (SNR) [11], [12].

Second, animals' thicker skin which typically has fur or scales on it, necessitating hair shaving for placing the devices and electrodes before each routine assessment. Third, when animals move freely, wearable devices need to be stuck onto the subject's body through tape or bandages. However, even with these securing measures, the weak attachment of the devices makes them susceptible to motion artifacts, impacting data accuracy [13]. Recently, injectable microchip implants, conventionally employed for animal identification, have shown its great potential as a promising alternative for monitoring animal health [14]-[17]. These injectable devices operating subcutaneously can improve coupling with tissue and enhance SNR compared to conventional wearables. Furthermore, the injectable devices can anchor firmly inside the body, which improves the device's immunity to motion artifacts.

Incorporating wireless power and data transmission techniques offers significant advantages for Injectable devices [18], [19]. Implementing wireless power and data transmission removes the need for batteries and wires, leading to a significant reduction in physical constraints, as well as device size and weight. This reduction, in turn, contributes to reducing the device's invasiveness and discomfort. Additionally, wireless injectable devices allow researchers to monitor the health of freely moving animals remotely. This wireless monitoring and data acquisition minimizes disruptions and stress on animals.

Given the constrained size and power budget of the injectable device, it is critical to incorporate an application-specific integrated circuit (ASIC) in it. The ASIC, in turn, can support multiple sensing modalities while maintaining a small area, fitting easily within the small injectable device. Recently, multiple multi-modal physiological monitoring ASICs have been designed [20]-[22]. These ASICs provide high SNR for each sensing modality but consume more power. Thus, they typically rely on a bulky battery for power, which prevents them from being assembled into a small implantable form factor. The work presented in [23], [24] introduces ASICs for wireless implantable devices that can record electrophysiological signals. These ASICs are low-power designs with a small area. However, they can only offer a single recording function, either PPG or ECG measurement, which cannot provide the necessary redundancy for animal health monitoring.

To address the limitations in existing ASIC and injectable device designs, in this paper, we expand upon [25], where we presented, for the first time, a wireless multi-modal physiological monitoring ASIC enabling subcutaneous body temperature, ECG, and PPG monitoring using an implant-sized injectable device, as depicted in Fig. 1b. Such multi-modal sensing capabilities offer crucial redundancy in capturing health metrics like heart rate (HR) and breath rate (BR), leading to less susceptibility to the effects of motion artifacts. Moreover, the simultaneous measurement of ECG and PPG offers pulse-transit-time (PTT), providing valuable data for future studies focused on analyzing this parameter animal health applications.

As shown in Fig. 1b, the device prototype houses the ASIC, two ECG electrodes for sensing ECG signal, and an light emitting diode (LED) and photodetector (PD) pair for PPG measurement, and a receiver (Rx) coil for receiving wireless power and transmitting data, all components within a cylindrical injectable device. The device has a 24 mm length and a 4 mm diameter. This miniature form factor reduces invasiveness and the risk of infection. Our efforts on device minimization include enhancing the ASIC integration and reducing off-chip components, such as utilizing a single coil for both wireless power and data transmission. To prevent tissue contamination,

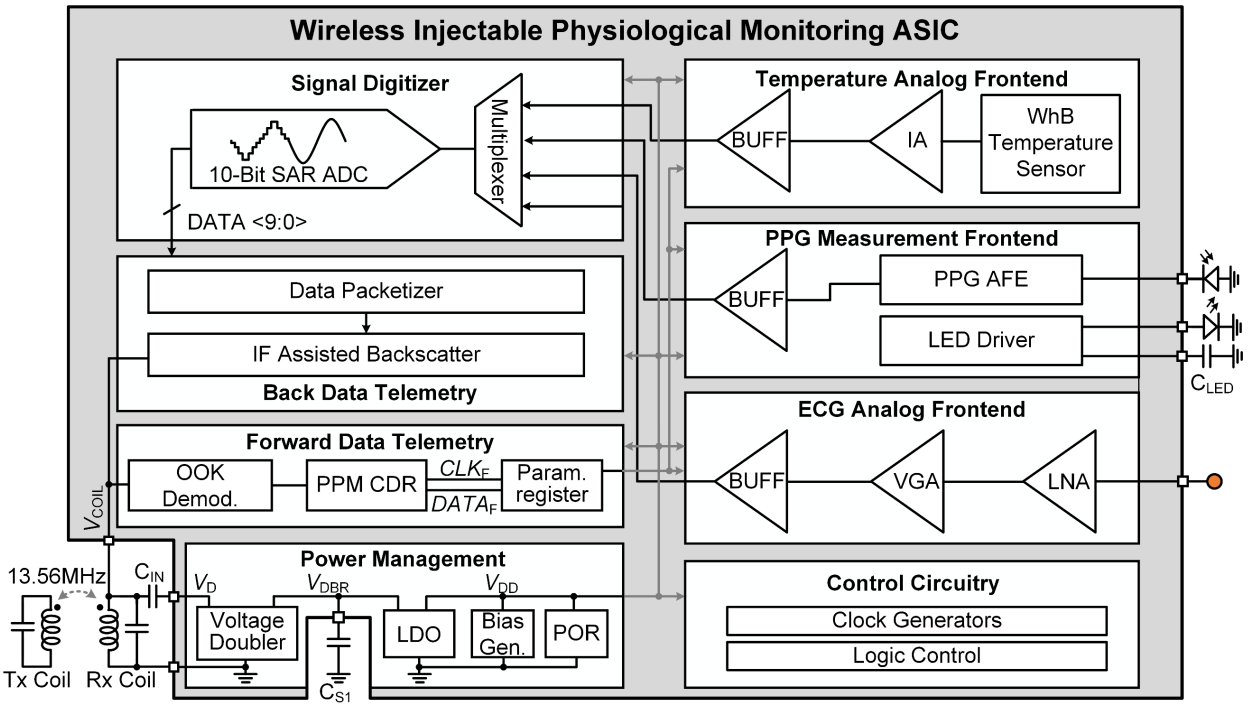

Fig. 2. System architecture of the wireless injectable multimodal physiological monitoring ASIC.

This article has been accepted for publication in IEEE Transactions on Biomedical Circuits and Systems. This is the author's version which has not been fully edited and content may change prior to final publication. Citation information: DOI 10.1109/TBCAS.2024.3372571

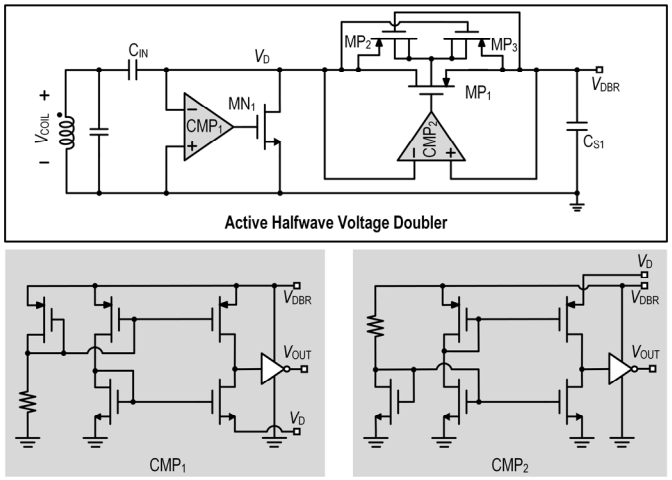

Fig. 3. Circuit diagram of the active voltage doubler.

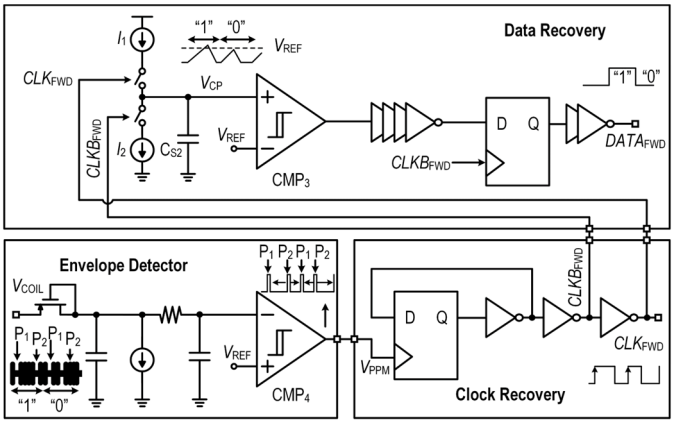

Fig. 4. Circuit diagram of the forward data telemetry.

we encapsulate the injectable device using epoxy glue, ensuring isolation from the surrounding tissue environment. The injectable device operates under the skin and receives power wirelessly via a 13.56 MHz inductive link. To avoid adding a separate data antenna, we utilize the same inductive link for transmitting and receiving wireless data. This wireless setup allows researchers to wirelessly acquire real-time data from the injectable devices during routine assessments, offering a more flexible approach to monitor animal health.

In this paper, Section II provides an overview of the proposed ASIC and its detailed circuit implementation. Section III details the electrical characteristics of the ASIC, derived from benchtop testing. Section IV focuses on evaluating the ASIC's functionality through *in vivo* experiments. Finally, the conclusion section offers a comparative analysis of the ASIC's performance and functionality against state-of-the-art designs, emphasizing the distinctive features of our proposed design.

II. The ASIC and Circuit Implementations

Fig. 2 depicts the architecture of the ASIC. The voltage doubler in the power management circuits converts the AC power, which is received by the Rx coil, to a 3.3 V supply voltage, V_{DBR}, a 1.8 V voltage, V_{DD}, biases and reference voltages. Once V_{DD} reaches a preset value, the power-on-reset (POR) will be triggered to enable forward data telemetry circuits. The user transmits configuration parameters to the ASIC to set up its physiological monitoring functions and corresponding analog frontends (AFE) through the forward data link. The user-defined parameters modulate the 13.56 MHz power carrier using on-off-keying (OOK). Simultaneously, the ASIC's forward data telemetry circuits demodulate the OOK-modulated Rx coil voltage, V_{COIL}, to decode the user-defined parameters. Then, the forward data telemetry circuits use these recovered parameters to program the AFEs for ECG, PPG, and body temperature measurements, adjusting settings like gain, bandwidth, and so on. The ECG AFE amplifies the ECG signal and filters out the undesired signals. To run PPG measurements, the LED driver delivers current pulses to activate the LED, while the PPG AFE amplifies the photodiode's output current resulting from the reflected light. The temperature AFE utilizes a resistor-based Wheatstone bridge (WhB) temperature sensor that converts the temperature variation to a voltage output, which is further amplified by the instrumental amplifier (IA). The output signals from the three AFEs are sequentially sampled and quantized by a 10-bit analog-to-digital converter (ADC) using successive approximation register-based (SAR) architecture. The back data telemetry serializes the ADC's output data and packetizes the data with headers before delivering data packets to the backscatter-based data transmitter (Tx) for transmitting the recorded data to the users. The control circuits generate clock signals and logic control signals required by the ASIC.

Fig. 3 shows the schematic of the active voltage doubler, along with two comparators, CMP_1, and CMP_2. Two power MOSFETs, MN_1 and MP_1, controlled by CMP_1 and CMP_2, respectively, turn on and off during different V_{COIL} phases. In the negative half cycle of V_{COIL}, CMP_1 turns on MN_1, while CMP_2 turns off MP_1, allowing V_{COIL} to charge the series capacitor, C_{IN}. In the positive half cycle of V_{COIL}, CMP_2 turns on MP_1 and CMP_1 turns off MN_1, doubling the voltage across the C_{IN} to charge the load capacitor, CS_1. To drive MN_1 and MP_1 at the high frequency of 13.56 MHz, we employed the common-gate comparator structure known for its high-speed attribute, which results from its low input impedance, minimal input capacitance, and simple structure [26]. Additionally, since MP_1 is implemented using PMOS transistors, we implemented a dynamic body biasing circuit, built by two auxiliary PMOS, MP_2 and MP_3, to switch the body voltage of MP_1 to the highest voltage between V_D and V_{DBR}.

We utilized the pulse-position modulation (PPM) technique presented in [27] to encode individual data bits by employing pairs of pulses. The pairs of pulses have a consistent period, with its commencement indicated by the first pulse, P_1. The different positions of the second pulse, P_2, within each period, represent different data bits. As shown in Fig. 4, the envelope detector first rectifies and filters the OOK-modulated V_{COIL}, and then compares the extracted envelope with a reference voltage to recover the PPM signal, V_{PPM}. The clock recovery circuit converts V_{PPM} to the clock signal, CLK_{FWD}. Afterward, the data recovery circuit extracts the data bit from V_{PPM} by alternatively charging and discharging a capacitor, C_{S2}. The rising edge and falling edge of CLK_{FWD} indicate the position of each first pulse and second pulse respectively. If P_2 is closer to the next P_1, I_1

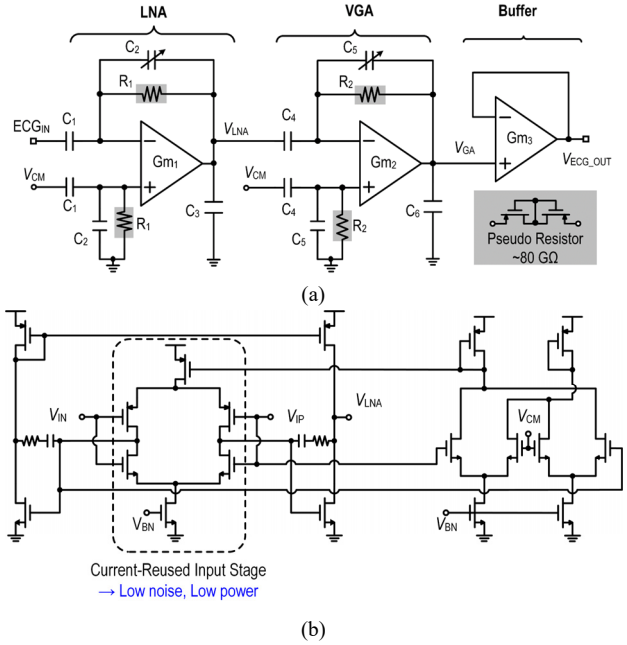

Fig. 5. Circuit diagram of (a) the ECG AFE and (b) Gm_1.

will charge C_{S2} for a longer time. Consequently, V_{CP} will exceed the V_{REF} during CLK_{FWD} is high, resulting in a $DATA_{FWD}$ =1 when the D-flip-flop samples the output of the comparator, CMP_3, at the falling edge of CLK_{FWD}. Conversely, if P_2 is closer to P_1 of the current pair, I_1 will charge C_{S2} for a shorter time. As a result, V_{CP} will not exceed the V_{REF} during CLK_{FWD} is high, leading to a $DATA_{FWD}$ =0. This PPM method is simple but robust. Moreover, as the user transmits the parameters only once and the pulse in PPM is narrow (10μs), this method features low power consumption and less interference on received wireless power.

The ECG AFE includes three cascaded amplifiers, as depicted in Fig. 5a [28]. The low-noise amplifier (LNA) includes a DC blocking capacitor, C_1, which not only blocks DC offsets in biopotential electrodes but also offers an infinite DC input impedance (Z_{IN}), preventing tissue damage caused by the DC current [29]. The LNA utilizes an inverting configuration where the midband gain is set by the ratio of C_1 to C_2. In addition, R_1 and C_2 set the high-pass corner, rejecting the low-frequency components below $1/(2\pi R_1 C_2)$. The pseudo-resistor, R_1, is implemented with a resistance level of giga-ohm to achieve sub-1 Hz low-cutoff frequency. We employ the symmetrical back-to-back structure to suppress the non-linearity of the pseudo-resistor [30], [31]. The transconductance operational amplifier (OTA), Gm_1, within the LNA employs an inverter-based input stage. This topology doubles the transconductance while maintaining the same bias current, leading to reduced input-referred noise (IRN) and higher energy efficiency (Fig. 5b) [32]. The size of input MOSFETs is sized to be large for decreasing the flicker noise. In order to provide additional gain while maintaining high dynamic range, we employ a variable-gain amplifier (VGA) following the LNA. Its gain can be set to 0-35 dB by programming the digital controlled capacitor array, C_5. Its bandwidth is also tunable, allowing for setting the high cut-off corner of the ECG AFE. The buffer provides additional low pass filtering to prevent aliasing artifacts and enough driving capability needed for the large

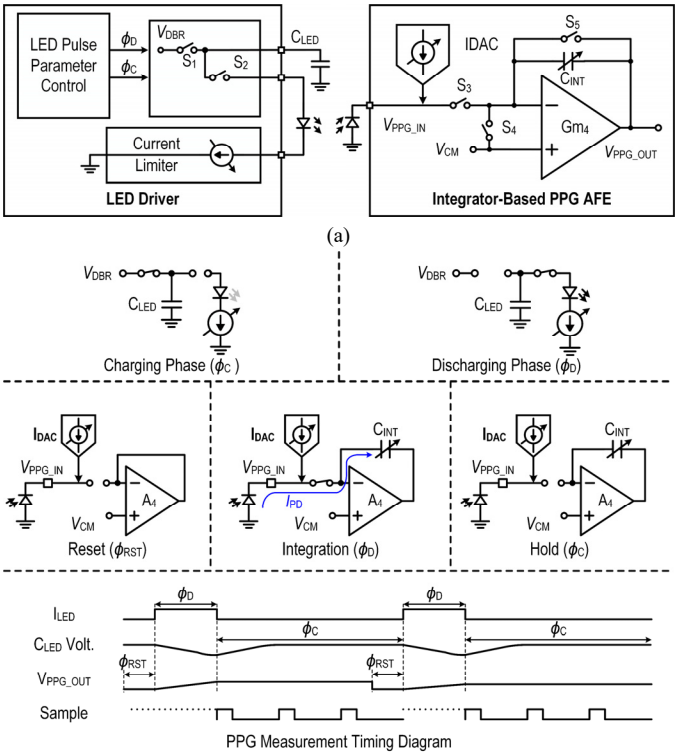

Fig. 6. (a) Circuit diagram of the PPG measurement frontend and (b) the timing diagram for PPG measurement.

capacitor array in the SAR ADC. The ECG AFE is designed with a gain between 45 dB and 80 dB and less than 5 μV_{RMS} input noise, allowing it to capture ECG signals ranging from 10 μV to 5 mV. A low cut-off corner below 0.5 Hz and an adjustable high cut-off corner of 100 – 600 Hz is chosen to cover the major signal band (i.e., 0.5 – 150 Hz) of ECG signals. This programmable high cut-off specification provides sufficient flexibility for ECG measurement. Setting a narrow bandwidth would help more effectively reject the high-frequency noise while a wider bandwidth can provide sufficient redundancy for time-domain analysis.

Fig. 6 presents the frontend circuit and timing control for the PPG measurement. During the charging phase, the LED driver closes S_1 and opens S_2, allowing a storage capacitor, C_{LED}, to be charged to V_{DBR}. Subsequently, in the discharging phase, the LED driver opens S_1 and closes S_2 to dump the charges in C_{LED}, delivering a large current pulse to illuminate the LED. The current pulses can be reconfigured to different LED current (I_{LED}) of 1-15 mA, pulse width of 50-200 μs, and frequency of 50-150 Hz. This frequency setting ensures the capture of the animal's heart rate, typically in the band of 6-8 Hz, using the PPG signal. The pulse width and I_{LED} specifications ensure adequate LED light intensity, allowing for the reflected light to be effectively detected by the PD. The AFE in PPG measurement frontend contains a 4-bit current digital-to-analog converter (IDAC) and a switched-capacitor (SC) integrator. The IDAC injects a variable 0.5-8 μA current to bias the DC voltage at the PD's output and compensate the offset in the PD current. The SC integrator converts the PD output current, I_{PD}, to a integration voltage, V_{PPG_OUT}, with a transimpedance gain of 2.5-40 MΩ. This transimpedance gain can be programmed by

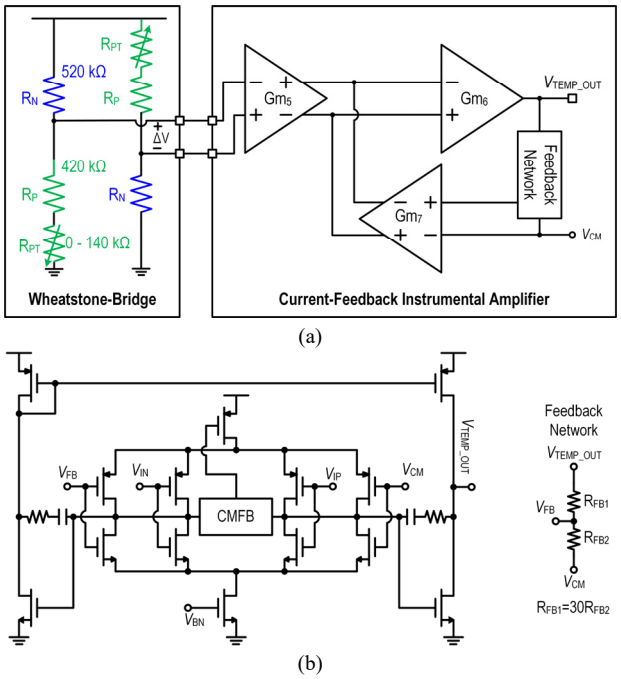

Fig. 7. Circuit diagram of (a) the temperature AFE and (b) the current feedback instrumentation amplifier.

tunning the duration of integration and the capacitance of the integration capacitor array, C_{INT} [33]. This transimpedance gain range is sufficient to detect I_{PD} values up to 720 nA. Before each time the LED is illuminated, the integrator resets the V_{PPG_OUT} to half of the supply voltage, V_{CM}, by closing S_5 and opening S_3 and S_4 during ϕ_{RST}. When the current pulse arrives, S_3 is closed while S_4 and S_5 are open. In this configuration, the I_{PD} is integrated into the C_{INT}, leading to a V_{PPG_OUT} equal to $(I_{PD}t_{INT})/C_{INT}$. After each current pulse, all switches are off, leaving the Gm_4 to hold the the integral voltage till the next reset phase. During the holding time, ϕ_C, the ADC takes samples of the integral voltage. Fig. 6b also shows the timing diagram of I_{LED}, C_{LED} voltage, V_{PPG_OUT}, and ADC sampling. This timing diagram demonstrates the entire PPG measurement operation. Such operation removes the needs for synchronizing ADC sampling with current pulses, simplifying the control logic design and permitting all AFEs to share a single ADC. This approach improves both power efficiency and area efficiency.

Fig. 7a shows the circuit diagram of the body temperature AFE. The WhB sensor contains two types of on-chip resistors with opposing temperature coefficients (TC). The R_N, implemented as a p-type poly resistor, has a negative TC, and the R_P, realized with n-type diffusion resistor, has a positive TC [34]. In this configuration, the open-circuit output voltage of the WhB is proportional to temperature. Then, a current feedback instrumentation amplifier (CFIA) amplifies the open-circuit voltage of the WhB, as shown in Fig. 7b. Given the CFIA's DC-input nature, it ensures an infinite input impedance, avoiding signal attenuation due to voltage division between the sensor and the CFIA [35]. To mitigate the impact of process variation-induced changes in the resistances of R_N and R_P on the temperature AFE's sensing range and accuracy, we employs a resistor array with 3 control bits, R_{PT}, for post-fabrication trimming. This implementation enhances the reliability of the WhB against process variations. The body temperature AFE is

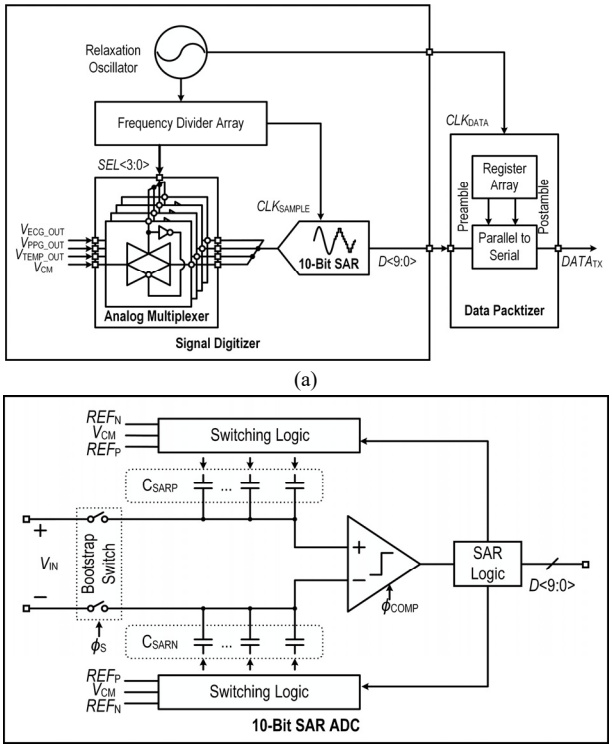

Fig. 8. Circuit diagram of the (a) signal digitizer and (b) 10-bit SAR ADC.

designed with a sensing range of 27 ˚C to 47 ˚C, accommodating the typical body temperature range of animals. Given the WhB sensitivity of 20 mV/˚C, we chose a gain of 30 dB for the IA to provide a resolution of 0.03 ˚C. This resolution is comparable to the state-of-the-art design [36].

Fig. 8a shows the circuit diagram of the signal digitizer. We implement a low-power RC-based relaxation oscillator that generates a 192 kHz signal, CLK_{DATA}. This signal is then input into a frequency divider array, producing two synchronized signals: an 8 kHz sampling clock, CLK_{SAMPLE}, and a 4-phase control signal bus, SEL<3:0>, with each control signal operating at 2 kHz. The 4-phase control signal bus controls the operation of the four transmission gates in the analog multiplexer, sequentially enabling each transmission gate to connect the corresponding AFE to the ADC for digitization. Each transmission gate is activated for a 0.5 ms time interval, during which the SAR ADC samples the each AFE output at the 8 kHz sampling clock. This process allows the SAR ADC to digitize each AFE output in a time-multiplexing manner. The ADC produces parallel data, which is serialized and packetized with an 8-bit preamble and a 6-bit postamble, resulting in 24 bits per package. This serial data stream is then delivered to back data telemetry circuits for wireless data transmission at the data rate of 192 kbps. Fig. 8 shows the schematic of the 10-bit SAR ADC. The ADC digitizes each AFEs' output in a time-multiplexing manner with a sampling rate of 8 kHz. In every sampling cycle, the bootstrap switch closes, allowing the input signal, V_{IN}, to be sampled onto the top plates of the capacitor DACs (C_{SARP} and C_{SARN}). Once sampling is complete, the digital conversion process of the SAR ADC begins. During each conversion cycle, the comparator compares the voltages on the top plate of C_{SARP} and C_{SARN}, generating the corresponding output code. The

This article has been accepted for publication in IEEE Transactions on Biomedical Circuits and Systems. This is the author's version which has not been fully edited and content may change prior to final publication. Citation information: DOI 10.1109/TBCAS.2024.3372571

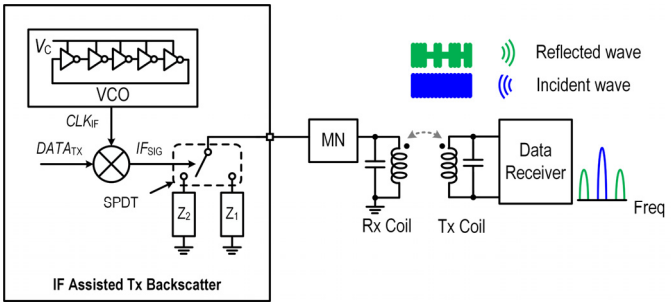

Fig. 9. Circuit diagram of the IF-assisted Tx backscatter.

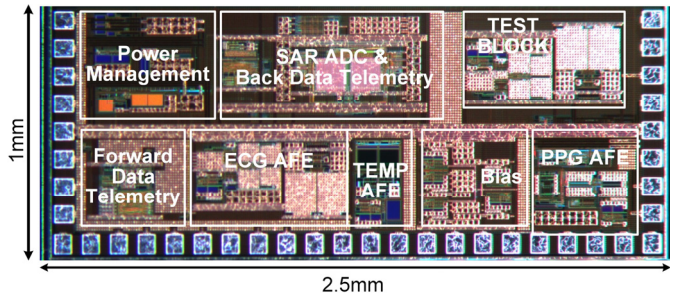

Fig. 10. The micrograph of the ASIC.

output code from the comparator drives the SAR logic circuits to switch the bottom plate of each capacitor in C_{SARP} and C_{SARN} among the reference voltages REF_P, V_{CM}, and REF_N. This action updates the top plate voltage of C_{SARP} and C_{SARN}, making them ready for the next cycle conversion. We adopted an energy efficient switching mechanism from [37]. Additionally, this switching mechanism can help reduce the required number of capacitors for C_{SARP} and C_{SARN} by 75%.

Fig. 9 illustrates the circuit diagram of data Tx. The data Tx employs load-shift- keying (LSK) backscatter scheme with an intermediate-frequency (IF)-assistance technique. The Tx data is first upconverted to an IF by mixing it with a 1 MHz IF clock, which is generated by a voltage-controlled oscillator (VCO). The IF signal, IF_{SIG}, drives a single pole double throw (SPDT) switch. Switching the SPDT switch would alternate the Rx coil's load between two different values Z_{L1} and Z_{L2}. Meanwhile, the reflection coefficient and the amplitude of the reflected wave are modulated. This two-step modulation scheme modulates the baseband signal to the two sidebands of the power carrier (i.e. 12.56 MHz and 14.56 MHz) [38]. Considering designing the data receiver, the strong power carrier can be filtered out using a notch filter while the baseband signal is preserved. This prevents the data receiver from being saturated by the power carrier signal. Consequently, data receiver design can be simplified by this IF-assisted LSK backscatter scheme.

III. Measurement Results

Fig. 10 shows the micrograph of the ASIC. The ASIC was fabricated in the TSMC 180nm standard CMOS process and occupies a total silicon area of 1 mm × 2.5 mm.

We characterized the power conversion efficiency (PCE) of the active voltage doubler using a vector network analyzer (VNA) with the input frequency set at 13.56 MHz [39]. The PCE is defined as the ratio between the voltage doubler's output power and its input power. Fig. 11a depicts the PCE under different load current (I_L) conditions with the peak efficiency of

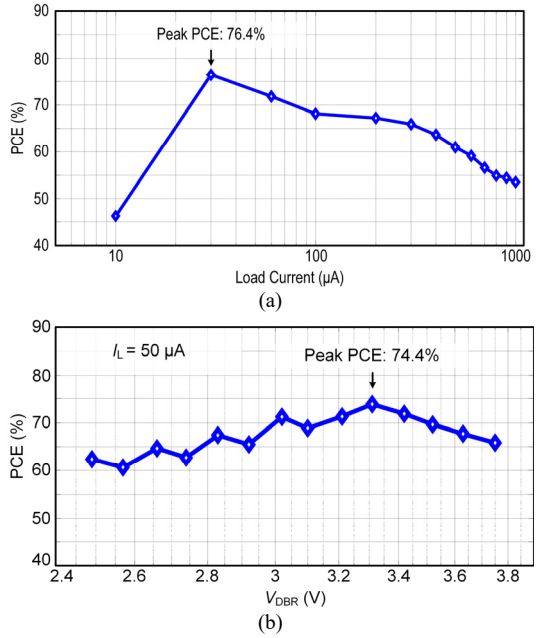

Fig. 11. Measured PCE of the active voltage doubler under different (a) load current and (b) output voltage.

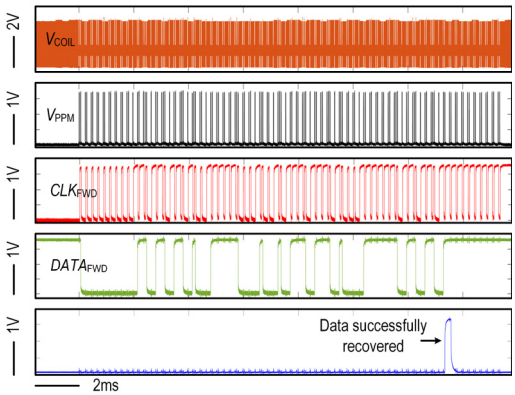

Fig. 12. Measured transient waveform of the forward data telemetry.

76.4% at I_L = 30 μA. We also evaluated the PCE against the voltage doubler output voltage, V_{DBR}, while maintaining a constant load current of I_L = 50 μA. As shown in Fig. 11b, the voltage doubler achieves a PCE of over 60% for V_{DBR} values between 2.4 V and 3.8 V, with the peak efficiency of 74.4% at V_{DBR} = 3.3V.

Fig. 12 presents the measured transient waveform of the forward data telemetry. V_{COIL} is modulated by pairs of PPM pulses, which encodes user commands. V_{PPM} represents the recovered PPM signal, which is subsequently recovered into the synchronized data, $DATA_{FWD}$, and the clock signals, CLK_{FWD}, by the data and clock recovery circuit. Afterwards, the $DATA_{FWD}$ is sampled by a serial-to-parallel circuit. When a data packet is successfully transferred and decoded, a flag signal is raised, indicating a successful data transmission and triggering the registers to capture the transmitted user commands.

We measured the frequency response and the input-referred noise (IRN) power spectrum density (PSD) of the ECG AFE, as presented in Fig. 13a and Fig. 13b, respectively. The ECG AFE consumes 5 μW power. The measured frequency response of the ECG AFE exhibits a bandpass characteristic with the low-

This article has been accepted for publication in IEEE Transactions on Biomedical Circuits and Systems. This is the author's version which has not been fully edited and content may change prior to final publication. Citation information: DOI 10.1109/TBCAS.2024.3372571

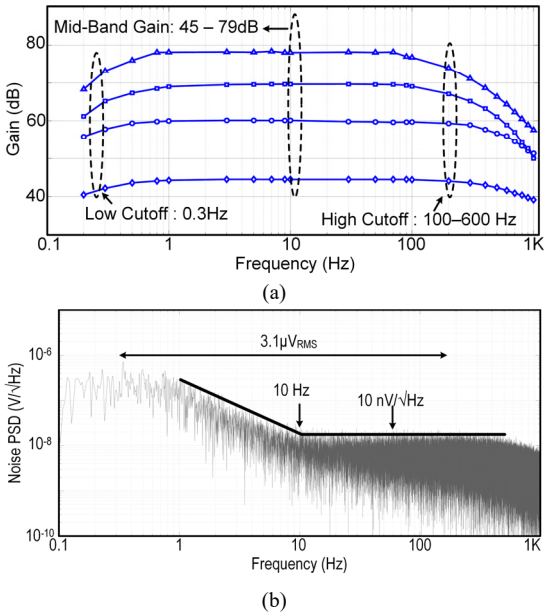

Fig. 13. Measured ECG AFE's (a) magnitude response over different frequency, gain, and bandwidth configuration and (b) noise power spectrum density (PSD).

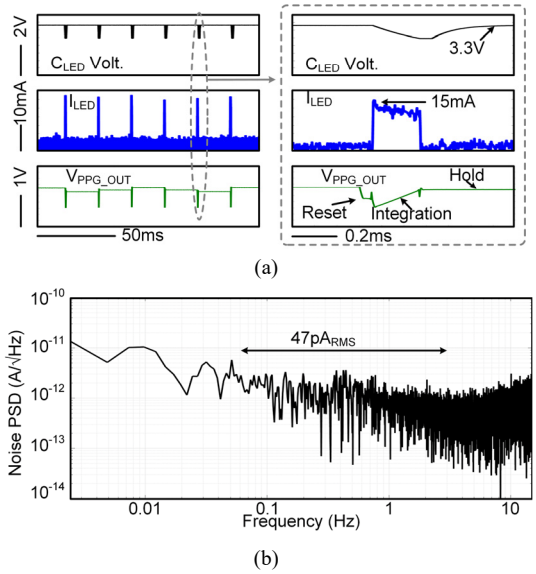

Fig. 14. Measured (a) transient waveforms of the PPG measurement results and (b) PPG AFE's input-referred noise spectrum.

cutoff corner at 0.3 Hz. Its midband gain can be programmed from 45 dB to 79 dB. In addition, the 3-dB bandwidth of the ECG AFE is tunable, ranging from 100 Hz to 600 Hz. The ECG AFE has an approximately 10 nV/ √ Hz thermal noise floor and a flicker noise corner at 10 Hz. Integrating the PSD from 0.3 Hz to 1kHz results in a 3.1 μV_{RMS} IRN.

Fig. 14a shows the measured transient waveforms of C_{LED} voltage, I_{LED}, and V_{PPG_OUT}, demonstrating the operation of PPG measurement. To measure I_{LED}, we connected a 50 Ω resistor in series with the LED and measured the voltage across the resistor. The LED is driven by current pulses with 200 μs pulse width at 50 Hz frequency. During each charging phase, the C_{LED} is charged to 3.3V to provide an LED driving voltage higher than the forward voltage. In the subsequent discharging phase,

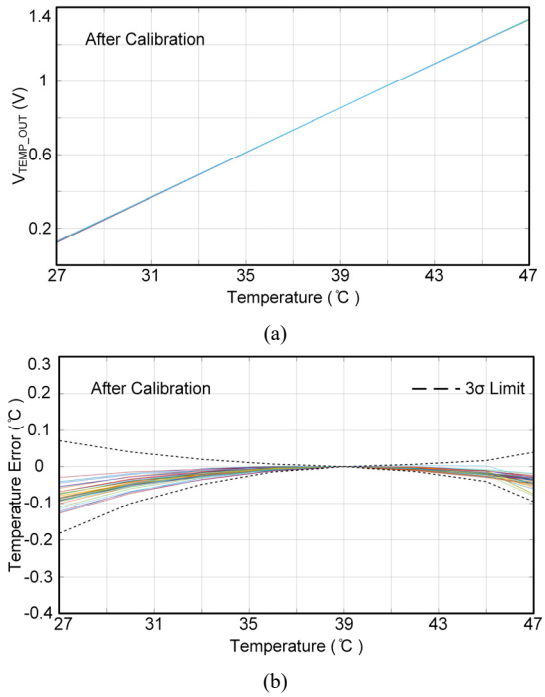

Fig. 15. (a) Measured output linear range of body temperature AFE; (b) inaccuracy over different temperature.

the C_{LED} dumps its charge, generating a 15-mA current pulse flowing through LED within 200 μs. The SC integrator resets V_{PPG_OUT} to V_{CM}, clearing the integration voltage of last PPG measurement. When the integration starts, the residual PD offset, which comes from the mismatch between PD offset and IDAC output current, may cause a voltage offset in V_{PPG_OUT}. However, this can be effectively calibrated during data processing. During the integration phase, I_{PD} charges the C_{INT}, converting the I_{PD} to an integration voltage. Afterwards, the SAR ADC samples the V_{PPG_OUT} before the next current pulse, during which the integration voltage is held by the PPG AFE. Figure 14b shows the PPG AFE's measured noise PSD, indicating an integrated IRN current of 47 pA_{RMS} over the bandwidth from 0.1 Hz to 10 Hz.

The body temperature AFE in twenty ASIC samples from the same die is characterized in a temperature-controlled oven. We first trim the process variation by manually tunning the 3-bit resistor array, R_{PT}. Afterwards, the AFE is trimmed at 39 ℃ to calibrate the offset. The AFE offered a temperature measuring range from 27℃ to 47℃ with an average power consumption of 12.6 μW, as shown in Fig. 15a. Fig. 15b shows that the inaccuracy of the body temperate AFE is about 0.2℃ (3σ) over the entire temperature measuring range. These measurement results indicates that this AFE offers accurate body temperature sensing with sufficient measuring range and high energy efficiency for the target application.

Fig. 16 shows the measured output power spectrum, differential non-linearity (DNL), and integral non-linearity (INL) of the 10-bit SAR ADC with an 8 kHz sampling rate. We fed through a 122.3 Hz sinusoidal signal with an amplitude of 720 mV_{PP} to the SAR ADC and collected 128k output data points for Fast-Fourier-Transform (FFT) analysis with a

This article has been accepted for publication in IEEE Transactions on Biomedical Circuits and Systems. This is the author's version which has not been fully edited and content may change prior to final publication. Citation information: DOI 10.1109/TBCAS.2024.3372571

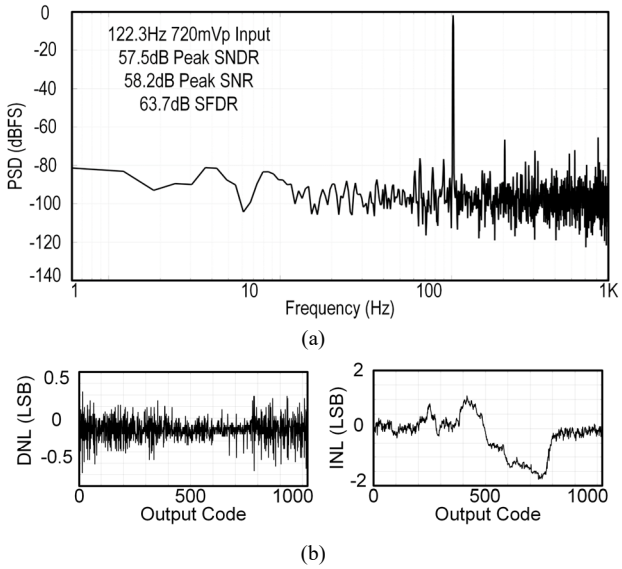

Fig. 16. Measured (a) output FFT PSD, (b) DNL, and INL of the 10-bit SAR ADC.

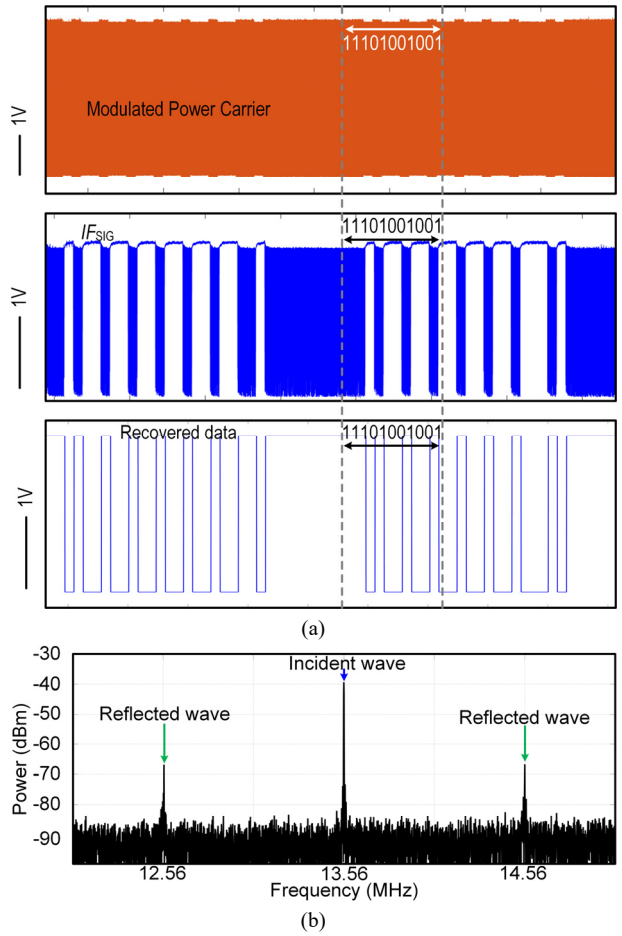

Fig. 17. Measured (a) transient waveforms of the IF-assisted Tx backscatter and (b) power spectrum at the data Rx side.

Hamming window. We also applied background calibration to mitigate the nonlinearity of SAR's capacitive DAC array. Within the DC to 1 kHz frequency band, the peak signal-to-noise-and-distortion ratio (SNDR), SNR, and spurious-free dynamic range (SFDR) are 57.5 dB, 58.2 dB, and 63.7 dB,

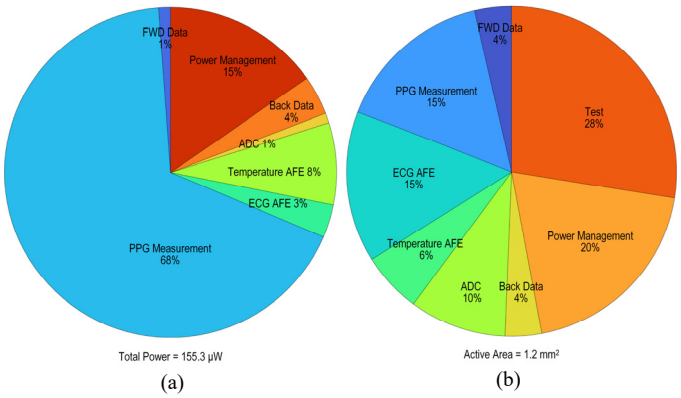

Fig.18. (a) Power breakdown and (b) area breakdown of the ASIC.

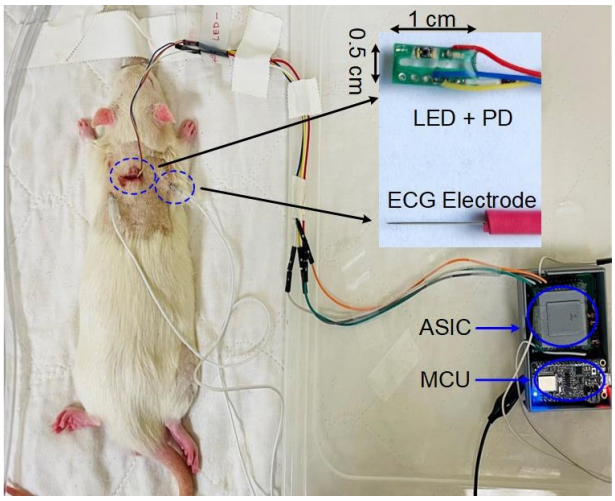

Fig. 19. *In vivo* experimental setup for evaluating ASIC's functionality on anesthetized rats.

respectively. The resultant effective number of bits (ENOB) is 9.3 bits. In Fig. 16b and Fig. 16c, the peak INL and DNL are within (+1.1, -1.7) least significant bit (LSB) and (+0.35, -0.37) LSB, respectively.

The measured transient waveforms in Fig. 17a demonstrate the IF-assisted LSK backscatter scheme in the time domain. IF_{SIG} is the IF-modulated baseband signal, which is further modulated onto the 13.56 MHz power carrier by switching the SPDT. At the data receiver side, we use a commercial software defined radio (SDR) to demodulate the reflected signal and recover the data. The data pattern observed from the measured signals are matched with each other, indicating successful data transmission. Fig. 17b shows the backscatter scheme in frequency domain. The measured spectrum indicates three signal tones located at 12. 56 MHz, 13.56 MHz, and 14.56 MHz respectively. This spectrum demonstrates that successfully translation of the baseband data to the sidebands of the power carrier.

The average power consumption of the ASIC is 155.6 µW, when ECG sensing, temperature sensing, and PPG measurement are enabled. Fig. 18a details the power breakdown of the ASIC. Notably, the PPG measurement accounts for 68% of the total power due to driving the LED at its maximum current of 15 mA. The active silicon area of the ASIC is 1.2 mm^2. When excluding the auxiliary test block, the power management block occupies

This article has been accepted for publication in IEEE Transactions on Biomedical Circuits and Systems. This is the author's version which has not been fully edited and content may change prior to final publication. Citation information: DOI 10.1109/TBCAS.2024.3372571

TABLE I: PERFORMANCE COMPARISON WITH STATE-OF-THE-ART MULTIMODAL PHYSIOLOGICAL MONITORING ASICS

Specifications		[20]	[23]	[24]	[21]	[22]	This Work
System	Technology	55 nm	180 nm	130 nm	55 nm	65 nm	180 nm
	Chip Area	2.5 mm × 1.8 mm	3 mm × 4 mm	3 mm × 2 mm	4.32 mm × 4.32 mm	3.1 mm × 1.6 mm	2.5 mm × 1 mm
	Power Source	Battery	Capacitive Link	15.7 MHz Inductive Link	Battery	N/A	13.56 MHz Inductive Link
	Forward Wireless Data	N/A	N/A	ASK	Bluetooth Low Energy	N/A	PPM-OOK (50 kbps)
	Backward Wireless Data	N/A	N/A	LSK Backscatter (22 kbps)	Bluetooth Low Energy	N/A	IF-LSK Backscatter (192 kbps)
	Power Consumption (μW)*	N/A	279.7	N/A	769	9.27	155.3
	Form Factor	Smart Watch	Implantable Devices	Implantable Devices	Chest Patch	Wearable Devices	Cylindrical Injectable Devices
	Sesnsing Modality	ECG/BIOZ/PPG	PPG	Elec. Recording/ Temp	ECG/BIOZ/PPG	ECG/Ozone/PPG	ECG/PPG/Temp
	ADC Architecture	Oversampling SAR	2nd order ΔΣ	8-bit SAR	Oversampling 13-bit SAR	N/A	10-bit SAR
ECG/ Elec. Recording	IRN (μV_{RMS})	0.73 (0.3 Hz -150 Hz)	N/A	7.79 (1 Hz -1 kHz)	0.7 (0.3 Hz -150 Hz)	20 (0.4 Hz - 45 Hz)	3.1 (0.3 Hz -1 kHz)
	Power (μW)	192.6	N/A	57.6**	40	0.165	5
PPG	IRN (pA_{RMS})	100*** (0.1 Hz -20 Hz)	162*** (0.1 Hz-10 Hz)	N/A	151/28 (0.1 Hz - 20 Hz)	45 (0.55 Hz -5 Hz)	47 (0.1Hz -10 Hz)
	Max I_{LED} (mA)	N/A	92.3	N/A	N/A	1.5	15
	Power (μW)	72 (AFE only)	279.7 (includes LED driver)	N/A	179/121 (includes LED driver)	9.032 (Includes LED driver)	105.6**** (includes LED driver)
	DR (dB)	130	108.2	N/A	111	92	75
Body Temperature	Range (℃)	N/A	N/A	0-50	N/A	N/A	27-47
	Resolution (℃)	N/A	N/A	0.12	N/A	N/A	0.03
	Inaccuracy (℃)	N/A	N/A	N/A	N/A	N/A	±0.2
	Power (μW)	N/A	N/A	36	N/A	N/A	12.6

*Includes the power of LED; **Includes the ADC's power consumption; ***Estimated; ****Measured power consumption with 15 mA LED current;

the most area, followed by the PPG measurement circuit and the ECG AFE.

Table 1 summarizes the performance metrics of the proposed ASIC. In addition, we compare the ASIC with the state-of-the-art ASIC designs for physiological monitoring wearable devices and implantable devices. To the best of our knowledge, this ASIC is the first design for a wireless, multi-modal, injectable health monitoring device. This ASIC enables subcutaneous ECG, PPG, and body temperature measurements simultaneously. The innovation of this ASIC lies at the following aspect: incorporating wireless power and data transmission, versatile physiological monitoring, high-level of integration, and tailored low-power circuit techniques. Compared to ASIC designs for wearable devices, the wireless operation of the proposed ASIC eliminates the need for bulky batteries and wires. This significantly reduces device discomfort and facilitates data acquisition during experiments, enabling long term health monitoring on freely moving animals. This is a key step towards the transformation of clinical use. When contrasted with ASICs designed for other implantable physiological monitoring devices, the proposed ASIC provides multiple sensing modalities, which ensures essential measurement redundancy and effectively mitigates the device's susceptibility to motion artifacts. This ASIC features high-level integration by combining the ECG AFE, PPG measurement frontend, body temperature AFE, ADC, wireless power management, wireless data Tx/Rx, and digital control circuit, all in a 2.5 mm × 1 mm silicon area. In addition, to reduce the power consumption, we tailored low-power circuits techniques for the ASIC. We employ low-power IF-assisted backscatter-based data transmitter. This technique removes the need for a power-hungry high-speed oscillators and power amplifier. In PPG measurement, we implement a SC LED driver to enhance energy efficiency of capacitor charging. Additionally, In PPG measurement, the SC integrator with integrate-and-hold operation removes the need for synchronizing ADC sampling with current pulses, simplifying the logic design and allowing one shared ADC to sample each AFE's output in a time-multiplexing manner. These innovations and characteristics collectively make the device highly suitable for animal health monitoring applications.

IV. *IN VIVO* VERIFICATION

We verified and evaluated the functionality and performance of the ASIC via an *in vivo* experiment. Fig. 19 shows the experiment setup. The animal model was 9-week-old adult Wistar rats (Rattus norvegicus) under isoflurane anesthesia. All animal procedures were approved by the Institutional Animal Care and Use Committee (IACUC) of NC State University. We subcutaneously inserted a PD-LED pair and ECG needle-electrodes into the rats' thoracic region on their dorsal side. The ASIC was mounted and connected to an evaluation board via wire-bonding. This board also contains necessary passive components such as storage capacitors. The microcontroller (MCU) encodes user commands into OOK pulses and modulates the power carrier, allowing the ASIC to

This article has been accepted for publication in IEEE Transactions on Biomedical Circuits and Systems. This is the author's version which has not been fully edited and content may change prior to final publication. Citation information: DOI 10.1109/TBCAS.2024.3372571

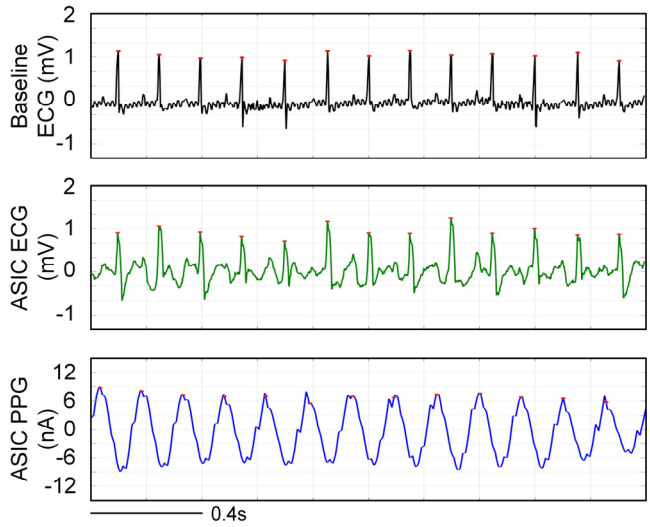

Fig. 20. Transient waveforms of Vernier EKG sensor-recorded baseline ECG signal, ASIC-recorded ECG signal and PPG signal.

wirelessly receive and configure each AFE. The commercial SDR (BladeRF, Nuand LLC) picked up the ASIC digitized and backscattered physiological signals wirelessly. The LED was driven with current pulses with a current of 10 mA, pulse width of 200 µs, and frequency of 150 Hz. According to our previous work [40], the increase in the local temperature of the rat's skin due to LED current is minimal, well below the safety limit of 0.5 °C [41]. We utilized a conventional gold-standard device (Go Direct™ EKG Sensor, Vernier Software & Technology) to simultaneously record the ECG signal alongside the ASIC. The ECG signal recorded by this commercial device serves as the baseline, which is utilized to verify and validate the performance and accuracy of the ASIC.

Fig. 20 illustrates the baseline ECG recorded by the commercial device, alongside the ASIC-captured ECG and PPG signals. Utilizing the peak detection algorithm [42], [43], we successfully extracted both HR and BR data from the three signals: the baseline ECG, the ASIC-recorded ECG, and the ASIC-recorded PPG. In Fig. 21a, the heart rates extracted from the baseline ECG and the ASIC-recorded ECG were 378.4±7.47 beats per minute (BPM) and 379.4±6.67 BPM, respectively, demonstrating a strong agreement between the two measurements. However, the heart rates extracted from the ASIC-recorded PPG were 390.2±9.49 BPM, slightly deviating (approximately 3%) from the baseline. This discrepancy may be attributed to motion artifacts including the breathing motion, which affect PPG signals more aggressively than ECG signals. However, incorporating multiple sensing methods in a device can potentially ensure redundancy for heart rate measurements and other health metrics. This multimodal approach would not only improve measurement robustness and accuracy but also mitigate the impact of artifacts on collected physiological data, enhancing overall system reliability and performance. As indicated in Fig. 21b, breath rates extracted from the baseline ECG, ASIC-recorded ECG, and the ASIC recorded-PPG were consistent at 57±5 breaths per minute (BPM), 57±3 BPM, and 57±4 BPM, respectively. The HR and BR across modalities demonstrate consistent results, confirming the ASIC's functionality and reliability. This emphasizes the ASIC's

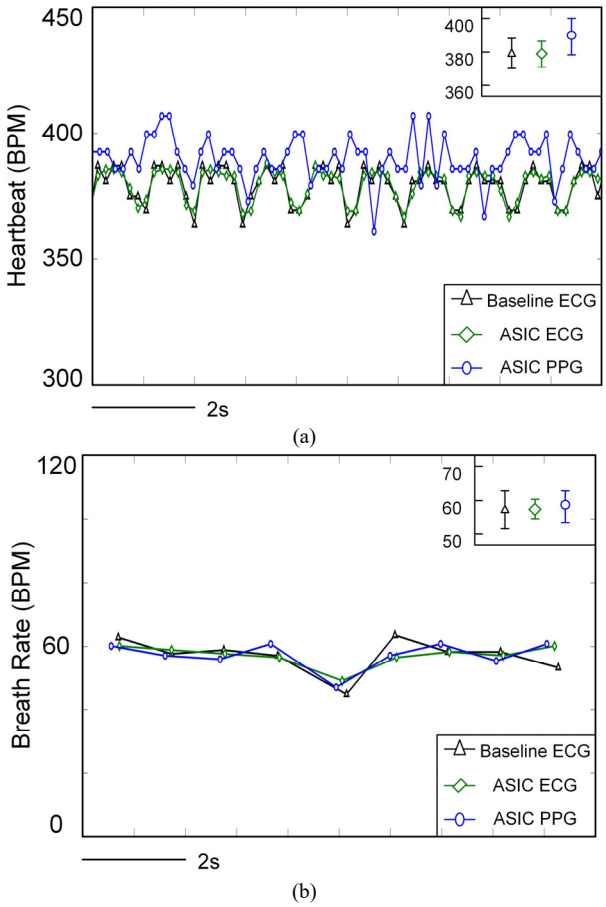

Fig. 21. The (a) heart rate and (b) breath rate extracted from baseline ECG, ASIC-recorded ECG, and ASIC-recorded PPG.

ability to monitor vital physiological parameters consistently and accurately, making it a valuable tool for animal use.

V. Conclusion

In this paper, we have introduced an ASIC with wireless operation and multimodal sensing for the injectable health monitoring device. The ASIC is fabricated in the 180 nm process with a size of 1 mm × 2.5 mm. The ASIC use the same link for both power and bidirectional data transmission, reducing the number of off-chip components and facilitating device miniaturization. The ASIC has multiple sensing modalities, including PPG measurement, ECG sensing, PPG, and body temperature monitoring. Multimodal sensing provides the necessary redundancy for physiological signal measurement and data collection, improving the ASIC immunity to motion artifacts. To realize the low power consumption of 155.3 µW, the AFE circuits are designed to be highly energy efficient while achieving the required performance in terms of noise level, bandwidth, gain, and linearity under limited power budget. Consuming an average power of 5 µW, the ECG AFE provides a gain range of 45 dB to 79 dB and IRN of 3.1 μV_{RMS} to effectively amplify the ECG signal. The PPG measurement frontend, featuring a switched-capacitor-based structure, can deliver up to 15 mA of LED current. Additionally, the SC integrator-based PPG AFE is capable of detecting PD currents up to 720 nA, with a transimpedance gain adjustable between 2.5 MΩ and 40 MΩ. The body temperature AFE senses

temperatures in the range of 27°C to 47°C with an accuracy of ±0.2°C. The 10-bit SAR ADC, with an ENOB of 9.3 bits, samples the output of each AFE sequentially at a rate of 8 kHz. The data packetizer serializes each ADC's sampled data and combines it with headers to generate a 24-bit data packet, resulting in a 192-kbps data rate. In addition, the data transmitter employs an IF-assisted backscatter scheme, which not only aids in realizing a low-power ASIC but also simplifies the data receiver design. A low-power ASIC not only facilitates wireless power transmission but also aids in device miniaturization. The low power consumption enables the use of a tiny coil for receiving wireless power, which in turn allows the assembly of the ASIC into a compact, injectable device. The functionality of the ASIC has been effectively validated through *in vivo* experiments conducted on anesthetized rats. The alignment of the measured breath rate and heart rate with the gold-standard demonstrates the reliable ECG and PPG recording enabled by our ASIC, showcasing the ASIC's promising potential for being a flexible, reliable, and robust tool in animal health monitoring applications.

ACKNOWLEDGEMENTS

The authors would like to thank Dr. Marnie Metzler, Sara McBride, Andrea Murr, and Sarah Kinlaw for their provision of veterinary equipment and performing animal procedures, and Dr. James Reynolds for his assistance during the in vivo experiment.

REFERENCES

[1] P. Ahmmed, J. Reynolds, A. Bozkurt, and P. Regmi, "Continuous Heart Rate Variability Monitoring of Freely Moving Chicken Through a Wearable Electrocardiography Recording System," *Poult. Sci.*, vol. 102, no. 2, p. 102375, Feb. 2023, doi: 10.1016/j.psj.2022.102375.

[2] S. I. Johnson, M. McMichael, and G. White, "Heatstroke in Small Animal Medicine: a Clinical Practice Review," *J. Vet. Emerg. Crit. Care*, vol. 16, no. 2, pp. 112–119, Jun. 2006, doi: 10.1111/j.1476-4431.2006.00191.x.

[3] P. J. O'Brien and J. S. Rand, "Canine Stress Syndrome," *J. Am. Vet. Med. Assoc.*, vol. 186, no. 5, pp. 432–433, Mar. 1985.

[4] D. Morton and P. Griffiths, "Guidelines on The Recognition of Pain, Distress and Discomfort in Experimental Animals and An Hypothesis for Assessment," *Vet. Rec.*, vol. 116, no. 16, pp. 431–436, Apr. 1985, doi: 10.1136/vr.116.16.431.

[5] H. J. Williams et al., "Identification of Animal Movement Patterns Using Tri-Axial Magnetometry," *Mov. Ecol.*, vol. 5, no. 1, p. 6, Dec. 2017, doi: 10.1186/s40462-017-0097-x.

[6] Q. Lin et al., "Wearable Multiple Modality Bio-Signal Recording and Processing on Chip: A Review," *IEEE Sens. J.*, vol. 21, no. 2, pp. 1108–1123, Jan. 2021, doi: 10.1109/JSEN.2020.3016115.

[7] J. Dieffenderfer et al., "Low-Power Wearable Systems for Continuous Monitoring of Environment and Health for Chronic Respiratory Disease," *IEEE J. Biomed. Health Inform.*, vol. 20, no. 5, pp. 1251–1264, Sep. 2016, doi: 10.1109/JBHI.2016.2573286.

[8] M. Konijnenburg et al., "A Multi(bio)sensor Acquisition System With Integrated Processor, Power Management, 8 × 8 LED Drivers, and Simultaneously Synchronized ECG, BIO-Z, GSR, and Two PPG Readouts," *IEEE J. Solid-State Circuits*, vol. 51, no. 11, pp. 2584–2595, Nov. 2016, doi: 10.1109/JSSC.2016.2605660.

[9] H. C. Ates, A. K. Yetisen, F. Güder, and C. Dincer, "Wearable Devices for The Detection of COVID-19," *Nat. Electron.*, vol. 4, no. 1, pp. 13–14, Jan. 2021, doi: 10.1038/s41928-020-00533-1.

[10] D. Son et al., "Multifunctional Wearable Devices for Diagnosis and Therapy of Movement Disorders," *Nat. Nanotechnol.*, vol. 9, no. 5, pp. 397–404, May 2014, doi: 10.1038/nnano.2014.38.

[11] D. J. Murphy, J. P. Renninger, and D. Schramek, "Respiratory Inductive Plethysmography as A Method for Measuring Ventilatory Parameters in Conscious, Non-restrained Dogs," *J. Pharmacol. Toxicol. Methods*, vol. 62, no. 1, pp. 47–53, Jul. 2010, doi: 10.1016/j.vascn.2010.04.006.

[12] W. Erhardt, C. Lendl, R. Hipp, G. Von Hegel, G. Wiesner, and H. Wiesner, "The Use of Pulse Oximetry in Clinical Veterinary Anaesthesia," *J. Assoc. Vet. Anaesth. G. B. Irel.*, vol. 17, no. 1, pp. 30–31, Jan. 1990, doi: 10.1111/j.1467-2995.1990.tb00385.x.

[13] S. Neethirajan, "Recent Advances in Wearable Sensors for Animal Health Management," *Sens. Bio-Sens. Res.*, vol. 12, pp. 15–29, Feb. 2017, doi: 10.1016/j.sbsr.2016.11.004.

[14] J. Reynolds, P. Ahmmed, and A. Bozkurt, "An Injectable System for Subcutaneous Photoplethysmography, Accelerometry, and Thermometry in Animals," *IEEE Trans. Biomed. Circuits Syst.*, vol. 13, no. 5, pp. 825–834, Oct. 2019, doi: 10.1109/TBCAS.2019.2923153.

[15] J. M. Valero-Sarmiento, S. Bhattacharya, A. Krystal, and A. Bozkurt, "Towards Injectable Biophotonic Sensors for Physiological Monitoring of Animals," in *IEEE SENSORS 2014 Proceedings*, Valencia, Spain: IEEE, Nov. 2014, pp. 503–506. doi: 10.1109/ICSENS.2014.6985045.

[16] P. Ahmmed, J. Reynolds, S. Hamada, P. Regmi, and A. Bozkurt, "Novel 3D-printed Electrodes for Implantable Biopotential Monitoring," in *2021 43rd Annual International Conference of the IEEE Engineering in Medicine & Biology Society (EMBC)*, Mexico: IEEE, Nov. 2021, pp. 7120–7123. doi: 10.1109/EMBC46164.2021.9630055.

[17] J. M. Valero-Sarmiento, P. Ahmmed, and A. Bozkurt, "In Vivo Evaluation of a Subcutaneously Injectable Implant with a Low-Power Photoplethysmography ASIC for Animal Monitoring," *Sensors*, vol. 20, no. 24, p. 7335, Dec. 2020, doi: 10.3390/s20247335.

[18] B. R. Bracio, W. Horn, and D. P. F. Moller, "Sensor Fusion in Biomedical Systems," in *Proceedings of the 19th Annual International Conference of the IEEE Engineering in Medicine and Biology Society. "Magnificent Milestones and Emerging Opportunities in Medical Engineering"* (Cat. No.97CH36136), Chicago, IL, USA: IEEE, 1997, pp. 1387–1390. doi: 10.1109/IEMBS.1997.756639.

[19] Y. Jia et al., "Position and Orientation Insensitive Wireless Power Transmission for EnerCage-Homecage System," *IEEE Trans. Biomed. Eng.*, vol. 64, no. 10, pp. 2439–2449, Oct. 2017, doi: 10.1109/TBME.2017.2691720.

[20] Y.-S. Shu et al., "A 4.5mm 2 Multimodal Biosensing SoC for PPG, ECG, BIOZ and GSR Acquisition in Consumer Wearable Devices," in *2020 IEEE International Solid- State Circuits Conference - (ISSCC)*, San Francisco, CA, USA: IEEE, Feb. 2020, pp. 400–402. doi: 10.1109/ISSCC19947.2020.9063112.

[21] S. Song et al., "A 769 µW Battery-Powered Single-Chip SoC with BLE for Multi-Modal Vital Sign Monitoring Health Patches," *IEEE Trans. Biomed. Circuits Syst.*, vol. 13, no. 6, pp. 1506–1517, Dec. 2019, doi: 10.1109/TBCAS.2019.2945114.

[22] R. Agarwala, P. Wang, H. L. Bishop, A. Dissanayake, and B. H. Calhoun, "A 0.6V 785-nW Multimodal Sensor Interface IC for Ozone Pollutant Sensing and Correlated Cardiovascular Disease Monitoring," *IEEE J. Solid-State Circuits*, vol. 56, no. 4, pp. 1058–1070, Apr. 2021, doi: 10.1109/JSSC.2021.3057229.

[23] F. Marefat, R. Erfani, K. L. Kilgore, and P. Mohseni, "A 280µW 108dB DR Readout IC with Wireless Capacitive Powering Using a Dual-Output Regulating Rectifier for Implantable PPG Recording," in *2020 IEEE International Solid- State Circuits Conference - (ISSCC)*, San Francisco, CA, USA: IEEE, Feb. 2020, pp. 412–414. doi: 10.1109/ISSCC19947.2020.9063116.

[24] T. Yousefi, K. Timonina, G. Zoidl, and H. Kassiri, "An Implantable Optogenetic Neuro-Stimulator SoC with Extended Optical Pulse-Width Enabled by Supply-Variation-Immune Cycled Light-Toggling Stimulation," *IEEE Trans. Biomed. Circuits Syst.*, vol. 16, no. 4, pp. 557–569, Aug. 2022, doi: 10.1109/TBCAS.2022.3198911.

[25] L. Zhao, R. G. Stephany, Y. Han, P. Ahmmed, A. Bozkurt, and Y. Jia, "A Wireless Multimodal Physiological Monitoring ASIC for Injectable Implants," in *ESSCIRC 2023- IEEE 49th European Solid State Circuits Conference (ESSCIRC)*, Lisbon, Portugal: IEEE, Sep. 2023, pp. 305–308. doi: 10.1109/ESSCIRC59616.2023.10268719.

[26] H.-M. Lee and M. Ghovanloo, "An Integrated Power-Efficient Active Rectifier with Offset-Controlled High Speed Comparators for Inductively Powered Applications," *IEEE Trans. Circuits Syst. Regul. Pap.*, vol. 58, no. 8, pp. 1749–1760, Aug. 2011, doi: 10.1109/TCSI.2010.2103172.

[27] H.-M. Lee, K. Y. Kwon, W. Li, and M. Ghovanloo, "A Power-Efficient Switched-Capacitor Stimulating System for Electrical/Optical Deep Brain Stimulation," *IEEE J. Solid-State Circuits*, vol. 50, no. 1, pp. 360–374, Jan. 2015, doi: 10.1109/JSSC.2014.2355814.

[28] Y. Jia et al., "A Trimodal Wireless Implantable Neural Interface System-on-Chip," *IEEE Trans. Biomed. Circuits Syst.*, vol. 14, no. 6, pp. 1207–1217, Dec. 2020, doi: 10.1109/TBCAS.2020.3037452.

[29] H. Chandrakumar and D. Markovic, "A High Dynamic-Range Neural Recording Chopper Amplifier for Simultaneous Neural Recording and Stimulation," *IEEE J. Solid-State Circuits*, vol. 52, no. 3, pp. 645–656, Mar. 2017, doi: 10.1109/JSSC.2016.2645611.

[30] R. R. Harrison and C. Charles, "A Low-power Low-noise CMOS Amplifier for Neural Recording Applications," *IEEE J. Solid-State Circuits*, vol. 38, no. 6, pp. 958–965, Jun. 2003, doi: 10.1109/JSSC.2003.811979.

[31] H. Rezaee-Dehsorkh, N. Ravanshad, R. Lotfi, K. Mafinezhad, and A. M. Sodagar, "Analysis and Design of Tunable Amplifiers for Implantable Neural Recording Applications," *IEEE J. Emerg. Sel. Top. Circuits Syst.*, vol. 1, no. 4, pp. 546–556, Dec. 2011, doi: 10.1109/JETCAS.2011.2174492.

[32] D. A. Hall, K. A. A. Makinwa, and T. Jang, "Quantifying Biomedical Amplifier Efficiency: The noise efficiency factor," *IEEE Solid-State Circuits Mag.*, vol. 15, no. 2, pp. 28–33, 2023, doi: 10.1109/MSSC.2023.3256353.

[33] Q. Lin et al., "A 134 DB Dynamic Range Noise Shaping Slope Light-to-Digital Converter for Wearable Chest PPG Applications," *IEEE Trans. Biomed. Circuits Syst.*, vol. 15, no. 6, pp. 1224–1235, Dec. 2021, doi: 10.1109/TBCAS.2021.3130470.

[34] S. Pan and K. A. A. Makinwa, "A 6.6- μ W Wheatstone-Bridge Temperature Sensor for Biomedical Applications," *IEEE Solid-State Circuits Lett.*, vol. 3, pp. 334–337, 2020, doi: 10.1109/LSSC.2020.3019078.

[35] B. J. Van Den Dool and J. K. Huijsing, "Indirect Current Feedback Instrumentation Amplifier with A Common-mode Input Range that Includes The Negative Roll," *IEEE J. Solid-State Circuits*, vol. 28, no. 7, pp. 743–749, Jul. 1993, doi: 10.1109/4.222171.

[36] A. Vaz et al., "Full Passive UHF Tag with a Temperature Sensor Suitable for Human Body Temperature Monitoring," *IEEE Trans. Circuits Syst. II Express Briefs*, vol. 57, no. 2, pp. 95–99, Feb. 2010, doi: 10.1109/TCSII.2010.2040314.

[37] X. Tong and Y. Zhang, "98.8% Switching Energy Reduction in SAR ADC for Bioelectronics Application," *Electron. Lett.*, vol. 51, no. 14, pp. 1052–1054, Jul. 2015, doi: 10.1049/el.2014.4112.

[38] D. Bharadia, E. McMilin, and S. Katti, "Full Duplex Radios," *ACM SIGCOMM Comput. Commun. Rev.*, vol. 43, no. 4, pp. 375–386, Sep. 2013, doi: 10.1145/2534169.2486033.

[39] U. Guler, Y. Jia, and M. Ghovanloo, "A Reconfigurable Passive Voltage Multiplier for Wireless Mobile IoT Applications," *IEEE Trans. Circuits Syst. II Express Briefs*, vol. 67, no. 4, pp. 615–619, Apr. 2020, doi: 10.1109/TCSII.2019.2923534.

[40] J. Reynolds, P. Ahmmed, and A. Bozkurt, "Preliminary Evaluation of an Injectable Sensor for Subcutaneous Photoplethysmography in Animals," in *2018 IEEE Biomedical Circuits and Systems Conference (BioCAS)*, Cleveland, OH: IEEE, Oct. 2018, pp. 1–4. doi: 10.1109/BIOCAS.2018.8584775.

[41] A. Bozkurt and B. Onaral, "Safety Assessment of Near Infrared Light Emitting Diodes for Diffuse Optical Measurements," *Biomed. Eng. OnLine*, vol. 3, no. 1, p. 9, Dec. 2004, doi: 10.1186/1475-925X-3-9.

[42] P. H. Charlton et al., "Breathing Rate Estimation from the Electrocardiogram and Photoplethysmogram: A Review," *IEEE Rev. Biomed. Eng.*, vol. 11, pp. 2–20, 2018, doi: 10.1109/RBME.2017.2763681.

[43] A. L. Jacobson, "Auto-threshold Peak Detection in Physiological Signals," in *2001 Conference Proceedings of the 23rd Annual International Conference of the IEEE Engineering in Medicine and Biology Society*, Istanbul, Turkey: IEEE, 2001, pp. 2194–2195. doi: 10.1109/IEMBS.2001.1017206.

Linran Zhao (Graduate Student Member, IEEE) earned a B.S. degree from the University of Electronic Science and Technology of China, Chengdu, China, in 2017, and later completed an M.S. degree at the University of California, Irvine, CA, USA, in 2019. Between 2019 and 2020, he worked as an Analog Design Engineer at ASML, San Jose. During the summer of 2022, he was an Analog Design Intern at Kilby Lab in Texas Instruments. Currently, Linran is pursuing a Ph.D. degree at The University of Texas at Austin, Austin, TX, USA. His research interests include high-energy-efficient ASICs for wireless neural interfaces, analog front-end and data converters for biomedical devices, as well as wireless systems for low-power IoT applications.

Raymond G Stephany has over 30 years of experience in CMOS design – predominantly in CPU design, memory design, and design-technology co-optimization. He was the Senior Fellow at AMD and the Senior Director at Qualcomm. His current research interests include analog I.C. circuit design, portable and injectable EEG and ECG sensing and stimulation circuit design, as well as low power, low noise, small area circuit design. He also enjoys cycling, hiking, astronomy, cabinet making, and working on his golf game.

Yiming Han (Graduate Student Member, IEEE) received his B.S. degree from the Dalian University of Technology in 2019 and his M.S. degree from Zhejiang University in 2022. He is now a Ph.D. student at the University of Texas at Austin. His research interests include analog/mixed-signal integrated circuits and wireless data transceivers for wearable and implantable devices.

Parvez Ahmmed (S'12--M'22) received the B.S. degree in electrical and electronic engineering from Bangladesh University of Engineering and Technology, Dhaka, Bangladesh, in 2014, and the M.S. and Ph.D. degrees in electrical engineering from North Carolina State University, Raleigh, NC, USA, in 2019 and 2021 respectively.

He is currently working as a postdoctoral research scholar with the Integrated Bionic MicroSystems (iBionicS) Laboratory, Department of Electrical and Computer Engineering, NC State University. His research interests include design of analog/mixed-signal circuits and integration of physiological sensors into low-power wearable and implantable systems for biomedical health monitoring applications.

Tzuping Huang (Graduate Student Member, IEEE) obtained his B.S. degree in Electrophysics from National Yang Ming Chiao Tung University in 2017, followed by his M.S. degree in Electrical and Computer Engineering from the same university in 2019. With 3 years of professional experience at Novatek, he worked as both a digital IC designer and a design verification engineer during different periods. Currently pursuing his Ph.D. at the University of Texas at Austin, his research focuses on mixed-signal integrated circuit design for biomedical applications.

Alper Bozkurt (S'01--M'10--SM'19) received the M.S. degree in biomedical engineering from Drexel University, Philadelphia, PA, USA, in 2004, and the Ph.D. degree in electrical and computer engineering from Cornell University, Ithaca, NY, USA, in 2010.

He is a Distinguished Professor with the Department of Electrical and Computer Engineering, North Carolina State University, Raleigh, NC, USA, where he is the Founder and the Director of the Integrated Bionic MicroSystems Laboratory. He is also the Co-Director of the National Science Foundation (NSF) Nanosystems Engineering Research Center for Advanced Self-Powered Systems of Integrated Sensors and Technologies (ASSIST) and the Institute of Connected Sensor Systems (IConS), NC State University.

Dr. Bozkurt received the Calhoun Fellowship from Drexel University, the Donald Kerr Award at Cornell University, the Chancellor's Innovation Award, and William F. Lane Outstanding Teacher Award at NC State University, the Best Paper Award from The U.S. Government Microcircuit Applications \& Critical Technology Conference and IEEE Body Sensor Networks Conference, the NSF CAREER Award, IBM Faculty Award and was included to the Popular Science Magazine 2015 Brilliant 10 list.

Yaoyao Jia (Member, IEEE) received the Ph.D. degree from Georgia Tech, Atlanta, GA, USA, in 2019. She is an Assistant Professor and the Fellow of Silicon Laboratories Endowed Chair in Electrical Engineering in the Chandra Family Department of Electrical and Computer Engineering at The University of Texas at Austin. Her research interests lie in analog and mixed-signal integrated circuits, power management integrated circuits, wireless power and data transmission, energy harvesting, and system integration for implantables, injectables, and wearables. She is the Associate Editor of IEEE TBioCAS and the TPC member of IEEE BioCAS, IEEE CICC, and ACM/IEEE DAC.